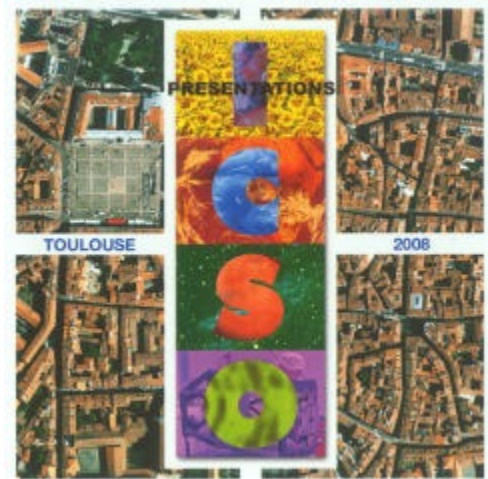


International Conference on Space Optics—ICSO 2008

Toulouse, France

14–17 October 2008

Edited by Josiane Costeraste, Errico Armandillo, and Nikos Karafolas



Characterization and cleaning control of optical coatings by using a goniometric light scatter instrument with sample imaging ability

Myriam Zerrad

Michel Lequime

Carole Deumié

Claude Amra



CHARACTERIZATION AND CLEANING CONTROL OF OPTICAL COATINGS BY USING A GONIOMETRIC LIGHT SCATTER INSTRUMENT WITH SAMPLE IMAGING ABILITY

Myriam Zerrad, Michel Lequime, Carole Deumié and Claude Amra

*Institut FRESNEL, UMR CNRS 6133
Université Paul Cézanne - Ecole Centrale Marseille
Domaine Universitaire de Saint-Jérôme, 13397 Marseille Cedex 20 (France)
<http://www.fresnel.fr/map2/diffusion/diffusion.php>*

E-mails : myriam.zerrad@fresnel.fr, michel.lequime@fresnel.fr, carole.deumie@fresnel.fr, claudio.amra@fresnel.fr

ABSTRACT

The principle of a new scattering measurement system including a mobile lighting and a fixed CCD array is described. This new system allows a spatially resolved light scattering characterization. Moreover it is possible to separate localized defects contribution from the local roughness measurement. The comprehensive characterization of optical coatings can be performed with this set-up, and some examples will be given.

Keywords: light scattering, CCD, surface roughness, cleaning control

1. INTRODUCTION

The recording of the Bidirectional Reflectance Distribution Function (BRDF) of optical components is widely used to quantify the amount of losses induced by scattering phenomena into the component and also to identify these losses origin (interfaces roughness, layers volume defects) [1-5].

When scattering originates from roughness surfaces, this measurement requires illuminating the sample with a laser beam at fixed incidence and recording the angular distribution of the scattered light intensity with a detector mounted on a rotating arm [6-10]. If this recording is achieved with a lighting beam whose diameter is comparable to the sample one, the presence of dust or localized scratches on the piece surface could alter the deduced roughness information. On the other hand, if the probe beam is tight focused, a 2D scan is necessary to achieve the complete surface characterization which leads to quite huge acquisition time.

To overcome this difficulty, we developed a new experimental set-up [11-13] whose detection arm is fixed at zero degree-incidence while the lighting arm becomes mobile around the sample. The detection system is a back illuminated scientific grade CCD which allows imaging the optical surface, sampling it by about one million of elementary pixels, reaching ultra low BRDF levels and recording the diffraction pattern

of any defect on the sample. This CCD-ARS instrument already provided comprehensive information on surface defects as well as measuring the correct intrinsic roughness, but this method should still be improved and its range of application extended.

In this communication, we will perform a quick presentation of the method and a detailed description of this new improved set-up and we will provide some examples of applications especially for the comprehensive characterization of low roughness surfaces (pixelized BRDF measurements with localization and size estimation of defects).

2. NUMERICAL ANALISYS

In this section, we will present a few numerical results illustrating our thought process and demonstrating all the interest of such a characterization method.

Our aim is not to develop here the exact procedure we used for our numerical simulations, first, because, it already has been detailed in previous publications [11], and then, because we prefer here focus our attention on the experimental set-up improvement. But, we think this step is necessary to understand the necessity of developing and improving such an experimental set up.

2.1 Impact of localized defects

Let us consider a low roughness plane silica surface shaped as a square (with side $L=500\mu\text{m}$) and illuminated by a collimated beam at wavelength $\lambda = 847$ nm in the air. These parameters have been chosen to well fit the experimental conditions of a standard light scattering measurement.

The surface profile is numerically generated to simulate a realistic surface and is expressed as an $N \times N$ matrix represented Fig. 1, with $N = 2L / \lambda$. Such a resolution ensures us the numerical simulations take care with surface variations in a spatial frequency range corresponding to the illumination wavelength.

On Fig. 1 is also plotted the BRDF calculated from this surface profile as a function of the scattering angle θ , in the incidence plane.

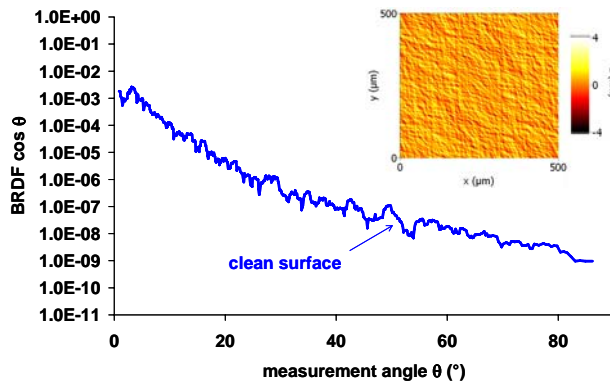


Fig. 1: BRDF calculated with first order theory from a synthetic low-roughness surface model

The rms roughness δ of the sample in the spatial range $\left[0, \frac{2\pi m_0}{\lambda}\right]$ can be deduced from the classical [14] relationship (1)

$$\delta^2 = \int_{\sigma} 2\pi\sigma\gamma(\sigma)d\sigma \quad (1)$$

where γ is the roughness spectrum of the surface and can be computed from the BRDF in the incidence plane by the relationship

$$BRDF \cos \theta = C(\theta)\gamma(\theta) \quad (2)$$

where $C(\theta)$ is a term derived from electromagnetic theory [4, 5] and θ , the measurement angle.

For the synthetic surface given Fig. 1, the relation ship (1) gives a rms roughness of 0.865 nm.

Let us numerically add to this surface some isolated dome shaped defects with random diameters between 3 and 8 μm and height less than 0.2 μm and whose refractive index is the same as the surface. The BRDF and, as a consequence, the rms roughness of the resulting surfaces will be affected.

As an illustration, you can see Fig. 2, the surface defined Fig. 1 with 10 localized defects and the corresponding BRDF whose level is obviously increased by the presence of these defects.

Moreover, we can see Fig. 3 the rms roughness of this same surface plotted as a function of the number of defects added on the sample surface.

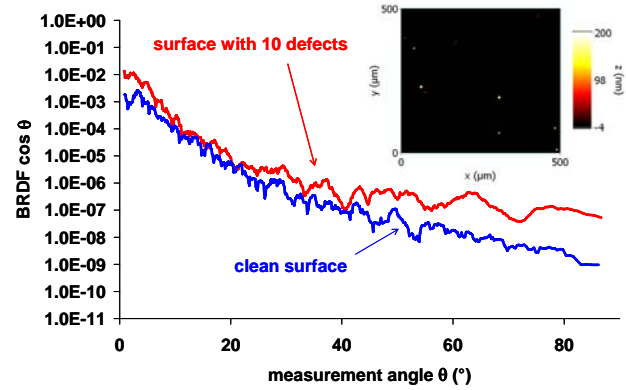


Fig. 2 : Influence of 10 localized dome shaped defects on light scattering from a 500 μm x 500 μm^2 surface

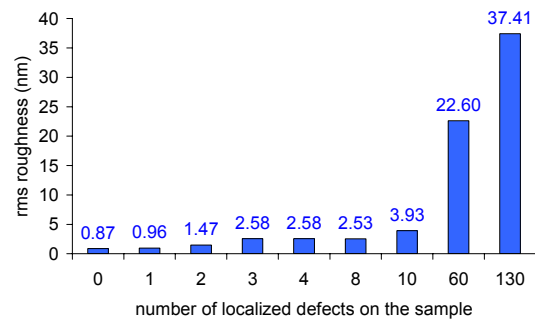


Fig. 3: rms roughness of the surface defined Fig. 1 with different numbers of isolated defects

We can see here that the presence of defects on the sample surface will perturb the scattering measurement on a significant way, even if the number of localized defects seems not to be significant.

These numerical results are showing the determination of the rms roughness of a surface through a scattered intensity measurement can very quickly become inaccurate because of the presence of a few localized defects on the surface. As it is obviously impossible to extract every defect from the sample, the only way for us to reduce the probability to find a defect on the analyzed area is to reduce the dimensions of this analyzed area.

2.2 Analyzed area reduction

To reduce the analyzed area, we divided the synthetic surface into smaller squares, each with a surface area 100 times smaller (i.e. 50 x 50 μm^2). It is done Fig. 4 for the surface defined Fig. 2. Two different cases then have to be analyzed: either the surface element is free of defects (in which case the observed scattering function is representative of intrinsic roughness, for example, elementary surface A, on Fig. 4, whose BRDF is given by the purple pattern), or it includes only one defect. In the latter case, the scattering function will be greatly affected and instantly recognizable as it is shown by the green pattern for elementary surface B.

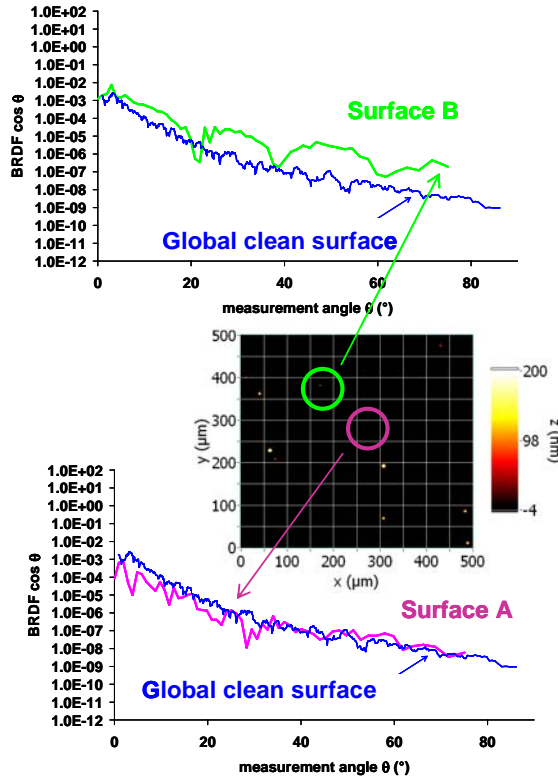


Fig. 4: Synthetic low-roughness surface with 10 defects defined Fig. 2 divided in 100 elementary $50 \times 50 \mu\text{m}^2$ surfaces.

BRDF of 2 elementary $50 \times 50 \mu\text{m}^2$ surfaces A et B compared with the BRDF of the full $500 \times 500 \mu\text{m}^2$ surface defect free defined Fig. 1.

If the elementary surface is defect free, the corresponding curve can be used to compute the rms roughness of the smaller region yields. For surface A, we obtain $\delta = 0.855 \text{ nm}$, which is very close to that determined for the whole surface in the same pulsation range, $\delta = 0.865 \text{ nm}$. On the other hand, the presence of a defect on the elementary surface is immediately identifiable by the presence of oscillations on the BRDF. In this case, the scattering function can closely be approximated by the Airy pattern corresponding to diffraction by the defect [15]. So that, lateral and axial dimensions of the defect can be deduced from the period and the amplitude of the oscillations. If the defect can be approximated by a circular stop of diameter $2a$, we can write:

$$BRDF \cos \theta \propto \left[\frac{J_1 \left(\frac{2\pi a}{\lambda} \sin \theta \right)}{\frac{2\pi a}{\lambda} \sin \theta} \right]^2 \quad (3)$$

Moreover, in the case of a single defect with diameter greater than the diffraction limit (i.e., 1.22λ), the scattering function will present one or more oscillations.

Its minima occur at specific scattering angles θ_m given approximately by

$$\sin \theta_m \approx \frac{Z_m}{\pi} \frac{\lambda}{2a} \quad (4)$$

where the Z_m are zeros of the J_1 Bessel function.

Now, the significance of reducing the dimensions of the analyzed area sounds as an obviousness. So, we have to define an optical set up allowing light scattering characterization of a whole sample dividing it in such a small surface.

To comprehensively characterize the roughness properties of a sample, we need to record the scattering function of each small surface element. If we consider a standard 1''-diameter optical substrate, and wish to characterize at least 80% of its surface, then about $M = 160,000$ $50 \times 50 \mu\text{m}^2$ surface elements will need to be scanned. This number is quite large, especially if we keep in mind that each BRDF acquisition requires from 20 to 100 angular positions (\mathcal{A}).

To rapidly record so many data points ($M \times \mathcal{A}$ is about 10 millions) while keeping a reasonable signal-to-noise ratio, some sort of multiplexed acquisition scheme is required. We chose to use spatial multiplexing by imaging the optical surface under testing in the focal plane of a CCD camera.

3. EXPERIMENTAL SET-UP

The use of a CCD spatial multiplexing scheme permits sampling of all surface coordinates simultaneously as long as we can guarantee stable relative positioning between the sample surface and the photodiodes of the array during the BRDF recording.

To guarantee this stability, we propose to fix the detection arm ($\theta=0^\circ$). The lighting arm becomes mobile instead, so that the incidence angle i can vary between a few degrees and 90 degrees. This choice leads to a new arrangement in which the position and orientation of the sample are constant relative to the detector. The sample is thus easily imaged on a CCD array. Moreover, we use a back-illuminated, scientific-grade CCD as the detector. This device samples about one million elementary pixels and is able to reach ultra-low BRDF levels thanks to the large integration time (up to 1 minute), enabled by the negligible dark current level.

Our first CCD-ARS set up already gave comprehensive information on surface defects as well as measuring the correct intrinsic roughness [11-13], but its range of application should still be extended. In this aim, the set up has been improved to allow the extension of:

- The measurement angular range using a new lighting system

- The analyzed area dimensions and resolution using a new detection system
- The background level of parasitic light using a new sample holder

We will present now these last evolutions.

A schematic representation of the new CCD-ARS instrument is given in Fig. 5.

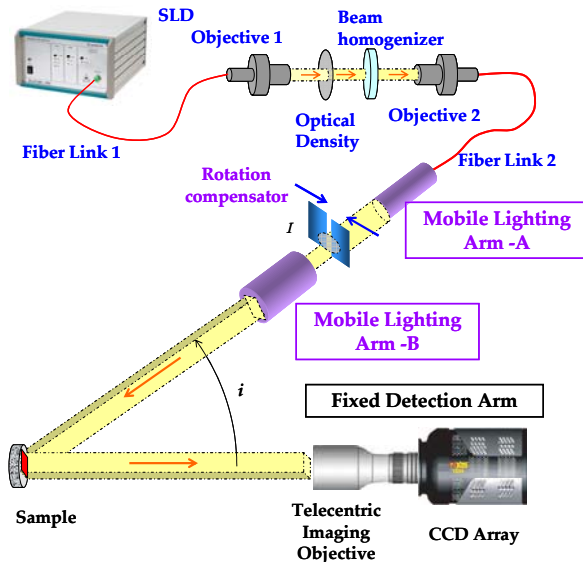


Fig. 5: the CCD ARS instrument

3.1 Lighting system

The light source is a high-power (15 mW) Super Luminescent Diode (SLD) centered at 840 nm, manufactured by Superlum[16]. Its spectral bandwidth ($\Delta\lambda=50$ nm) is large enough to cancel the far-field speckle typical of coherent laser lighting, yet quite similar to the monochromatic configuration assumed by our numerical simulations. The first fiber link is a standard single-mode fiber, while the second is an all-silica, step index multimode fiber with core diameter $2a = 600 \mu\text{m}$ and numerical aperture $\sin \alpha = 0.25$. The two links are coupled via a pair of objectives. A beam homogenizer and a motorized wheel are installed between these two objectives, to uniform the lighting beam and adjust the light power with an optical density (0, 1, 2 or 3).

A key point of this new set up lays in the conception of the lighting system. It is installed on a mechanical arm that rotates (by angle i) around the sample. (The axis of this rotation is vertical, and lies in the front face of the sample). This lighting arm is divided in two parts (part A and B on Fig. 5). Part A is a telecentric objective which will provide a magnified image I (the magnification is 10) of the multimode fiber's extremity which is located in its focal plane. Part B is an other telecentric objective which will image the intermediary

image I on the sample surface with a magnification $M = 3.75$). So, the illuminated area on the sample is a 22.5mm diameter disk at normal incidence. More accurately, it is an ellipse whose major axis is inversely proportional to $\cos i$, so that, for incidence angles higher than 25° , the area illuminated is larger than the sample diameter. It can have a troubling effect on the background level for low-roughness samples.

To avoid the extension of the illuminated area during the scan, we added to the lighting arm a rectangular diaphragm with a tunable aperture which will compensate the rotation effect on the spot by continuously morphing the beam. It is positioned on the image focal plane of image I .

The lighting arm rotates on the horizontal plane, so the vertical dimension of the diaphragm stays $15.9/M = 4.2$ mm during the whole scan. The horizontal aperture L of the diaphragm is defined as a function of the incidence angle i by the relationship:

$$L = \frac{15.9}{M} \cos i \quad (5)$$

With this rotation compensator, the shape of the illuminated region is a constant 15.9 mm side square during the angular scan and the scan limit can reach 85° . For incidence angles higher than 85° , the side of the sample holder is hiding a part of the beam.

So, with the lighting system we designed, a 25mm diameter sample will be illuminated with incidence angles from 13 to 85° with a spot shaped as a 15.9 mm side square.

Let us now define the detection system.

3.2 Detection system

The surface of the sample is imaged by a Princeton Instruments PIXIS 1024B camera[17] which uses a back-illuminated, scientific-grade CCD with a 1024 x 1024 imaging array (square pixels with side $p = 13 \mu\text{m}$).

The imaging objective is a custom telecentric lens from Light Works^[18], with magnification $G = 0.5$, a working distance of 400 mm, and a nominal aperture number of 16 (N). We stress that the telecentric objective is a key element defining the characteristics of our instrument. In a telecentric objective the entrance pupil is rejected at infinity, which guarantees that the angular coordinates of the chief ray defining the direction of scattered light are the same at all points on the sample surface. This property is illustrated in Fig. 6.

It is important to note here that the use of a high F-number telecentric objective coupled with a tightly collimated lighting beam is a key point of our set up. It is thanks to these two elements that our experiment provides accurate light scattering measurements instead of simple surface imaging.

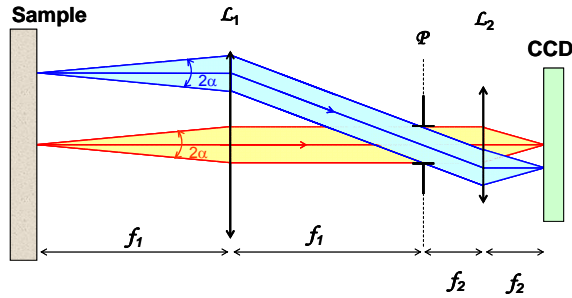


Fig. 6: The working principle of a telecentric objective used as an imaging device

3.3 Sample holder

Our detection system is so sensitive that any element on the light trajectory can become a source of parasitic light and perturb the scattering measurement. So, to record the BRDF sample in optimal conditions, the scan will have to be performed with a sample holder perfectly invisible for the CCD-ARS set up. To approximate this objective, we designed a new sample holder whose visible surface is drastically reduced.

A schematic of this sample holder is given Fig. 7-a. It is a 25 mm diameter ring with a 1 mm thickness united with a second 1mm thick ring whose internal and external diameters are respectively 22.5 and 26mm. The sample is held by the first ring by pressure effect and blocked by the second ring. The whole sample holder is black anodized to limit the amount of possible stray light and it is linked by three threads to an external support which is far (more than 30 cm) from both the field of view of the detection system and the illuminated area. With such a sample support, the visible part of a 25 mm diameter sample is a 22,5 mm diameter circle.

You can see Fig. 7-b an image recorded with a 25 mm diameter ZnSe sample illuminated with a lighting angle $i = 13.5^\circ$ by the square shaped beam defined section 3.1 and maintained by the sample holder described section 3.3. As it can be seen, the sample holder seems nearly invisible for the detection system.

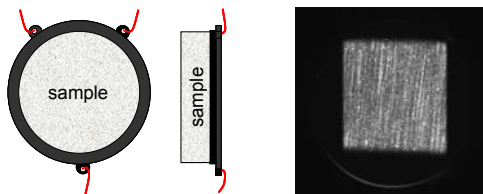


Fig. 7 -a: sample holder, schematic front and side views
-b: image recorded with a ZnSe sample in our final measurement configuration

4. APPLICATIONS

4.1 Perfect diffuser

The characterization of a perfect diffuser is necessary to calibrate our CCD-ARS instrument. Fig. 8 shows a

sequence of images recorded by the CCD array for incidence angles from 13.5 to 90 degrees. As expected, the illuminated area keeps the same square shape.

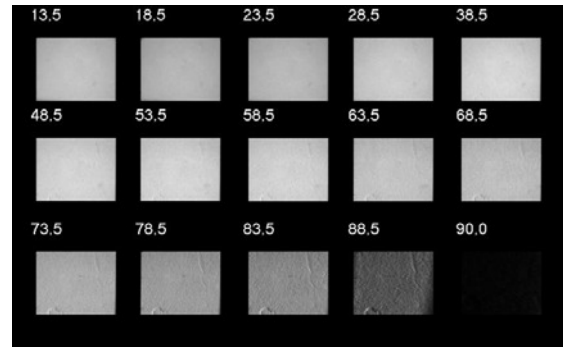


Fig. 8: CCD images recorded with a perfect diffuser.

The instrument can be calibrated for each pixel of the illuminated area. The angular response $G(i)$ is recorded for each pixel, and then it is fitted by the theoretical response of a perfect diffuser.

$$BRDF \cos i = \frac{1}{K} \frac{G(i)}{\tau} \cos i = \frac{\rho}{\pi} \cos i \quad (6)$$

where τ is the integration time and ρ the albedo of the perfect diffuser.

The calibration constant K is adjusted by a least-squares method for each pixel and allows the conversion from the image grey levels to the BRDF of the sample.

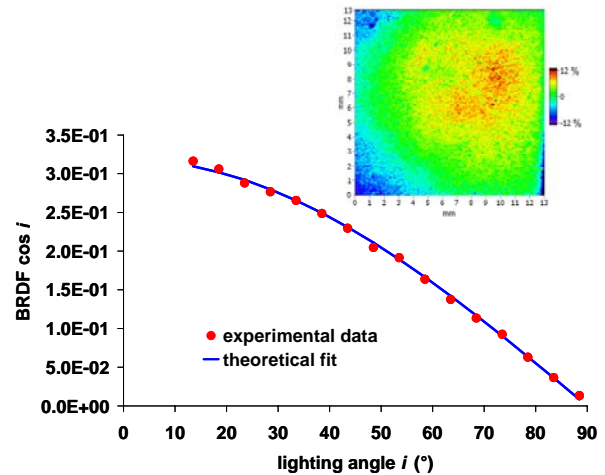


Fig. 9: angular response of a perfect diffuser. Experimental data compared with the theoretical response and relative variation of the calibration constant K computed from a perfect diffuser scan at each pixel position within a 13 mm square

Fig. 9 shows the values obtained for this calibration constant (K) for each CCD pixel inside a 13 mm square and the scattered light intensity recorded during the angular scan for one pixel, selected at random. The data are well fit by the theoretical response of a perfect diffuser. For all pixels inside the initially illuminated

area, we obtain a similar level of agreement. This result confirms the validity of our measurement method.

4.2 Instrument signature measurement

A signature measurement is the lowest level of BRDF measurable with a given Instrument. It is equivalent to the BRDF of an ideal, scatter-free sample due to instrument limitations. In our case, the signature was determined by removing the sample and otherwise measuring the effective BRDF under the same conditions that would later be used in actual sample measurements. Accordingly, the incident angle varied between 13.5° and 90° , the optical density was set to zero, and the integration time was 200 seconds.

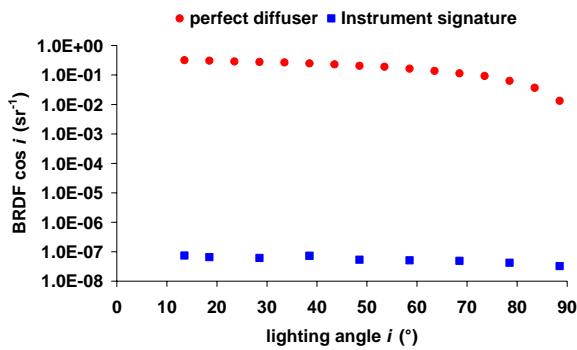


Fig. 10: CCD-ARS instrument signature

The equivalent BRDF level varied from $7 \times 10^{-8} \text{ sr}^{-1}$ at 13.5° to $3 \times 10^{-8} \text{ sr}^{-1}$ at about 90° . The rms noise under these conditions is less than 10^{-9} sr^{-1} . The instrument signature is therefore dominated by stray light and Rayleigh scattering. Fig. 10 compares the result of this measurement to that achieved on a perfect diffuser.

4.3 Germanium wafer

To complete our evaluation of the CCD-ARS instrument and demonstrate its efficiency at locating isolated defects, we examine a low-roughness germanium wafer with some surface particles (due to imperfect cleaning or eventual polish scratches). The whole CCD image at a lighting angle of 13.5° is shown in Fig. 11. The intensity of the lighting beam is maximal (zero optical density) and the integration time is 10 seconds. In the saturated zones (solid white) excess photo-electrons flow over to surrounding pixels, usually in the same column. Obviously, the BRDF measurement can not be achieved in these regions of the CCD array.

First, we measured scattered light within a larger test area 2 mm square defined Fig. 11. An enlarged view of this test area is shown in Fig. 11. To have a better visualisation of the surface defects, an inverted 16-bit logarithmic scale is chosen for the representation. The displayed surface has typically the dimensions of areas characterized by standard BRDF measurements. In standard configurations, the BRDF recorded would be the global BRDF of this region obtained by averaging

over all pixels. It is plotted in Fig. 12. We can see it does not exhibit any oscillations whatsoever.

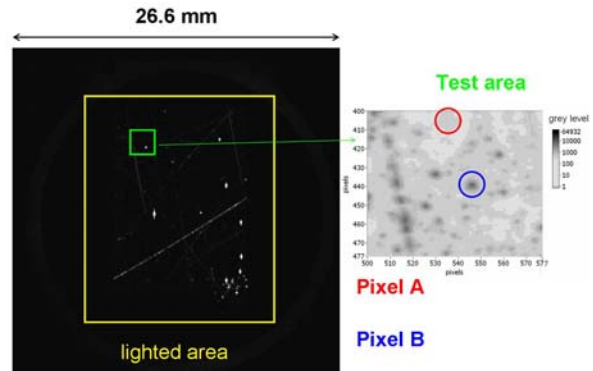


Fig. 11 : Ge wafer imaged with the CCD-ARS instrument and enlarged view of the 2 mm square test area

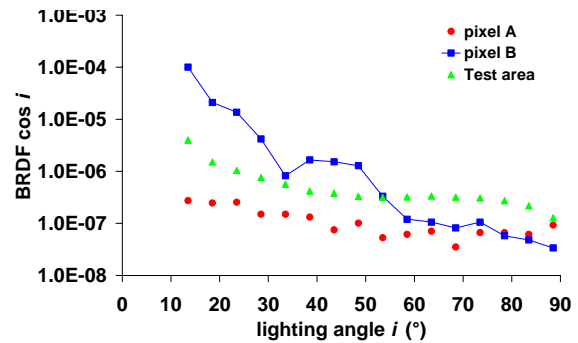


Fig. 12: Cosine-corrected BRDFs of selected pixels (pixel A: without a defect; Pixel B: with a single defect; Test area : a $2 \times 2 \text{ mm}^2$ square area)

With our CCD-ARS set up, this $2 \times 2 \text{ mm}^2$ region is divided in $77 \times 77 = 5929$ elementary pixels and we acquire the BRDF of each one of these 5929 elementary surfaces. For example, in Fig. 12, we plot the BRDF of two elementary surfaces selected within the global surface displayed Fig. 11. The pixel labelled A on Fig. 11 is associated with a surface element which seems free of particles. The BRDF of this surface element, shown in Fig. 12, is a gradually decreasing function of angle. Its mean level is about 10^{-7} sr^{-1} , which is 5 times greater than the instrument signature and 5 times lower than the level recorded with a standard BRDF measurement. In contrast, the pixel labelled B on Fig. 11 is associated with a surface element which clearly contains a small and isolated defect. The shape of the BRDF presents oscillations. It is clearly characteristic of diffraction from a small stop[15].

These results are in perfect accordance with the numerical simulations presented in Section 2 (see especially Fig. 2 and Fig. 4). It also illustrates the kind of erroneous information that can be produced by classical BRDF instruments when the surface topology includes localized defects[15, 19].

4.4 Conclusion and perspectives

This paper has been devoted to the description of the last improvements of the CCD-ARS set up developed at the Institut Fresnel for measuring the scattered light function of a low-roughness surface. The application range of the instrument has been outstandingly improved. First, the angular range has been extended in order to reach angles from 65° to 90° by designing an original lighting system which provides a constant square shaped spot on the sample surface during the whole scan. Furthermore, an atypical sample holder has been achieved and, coupled with the new lighting system, it reduces drastically the parasitic light.

This new instrument can provide comprehensive information on surface defects as well as measuring the correct intrinsic roughness. The number of useful data points acquired during a single scan using this device can easily reach several millions. The positions and sizes of defects can be determined from obvious features of the scattered light profile in each CCD pixel. This apparatus can therefore be used to efficiently compare and qualify optical coating cleaning procedures or deposition processes.

Finally, the theoretical principles behind this roughness measurement method are clearly compatible with other spectral studies (wavelength switching of incoherent sources) and polarization analysis, as previously defined by our team on a standard ARS instrument [20-22].

REFERENCES

[1] Bennett, J. M. and Mattson, L., "Introduction to surface roughness and scattering, 2nd Ed," in *OSA*, Washington DC (1999).
[2] Amra, C., "From light scattering to the microstructure of thin-film multilayers," *Appl. Opt.* 32(28), 5481 (1993)
[3] Duparré, A. and Kassam, S., "Relation between light scattering and the microstructure of optical thin films," *Appl. Opt.* 32(28), 5475-5480 (1993)
[4] Amra, C., "Light scattering from multilayer optics. II. Application to experiment," *J. Opt. Soc. Am. A* 11(1), 211 (1994)
[5] Amra, C., "Light scattering from multilayer optics. I. Tools of investigation," *J. Opt. Soc. Am. A* 11(1), 197 (1994)
[6] Amra, C., Grezes, B. C., Roche, P. and Pelletier, E., "Description of a scattering apparatus: application to the problems of characterization of opaque surfaces," in *Applied Optics. 15 July 1989; 28(14): 2723-30* (1989).
[7] Roche, P. and Pelletier, E., "Characterizations of optical surfaces by measurement of scattering distribution," *Appl. Opt.* 23(20), 3561-3566 (1984)

[8] Germer, T. and Asmail, C., "Goniometric optical scatter instrument for out-of-plane ellipsometry measurements," *Review of Scientific Instruments* 70(9), 3688-3695 (1999)
[9] Duparre, A., Ferre, B. J., Gliech, S., Notni, G., Steinert, J. and Bennett, J. M., "Surface characterization techniques for determining the root-mean-square roughness and power spectral densities of optical components," *Applied Optics* (2002)
[10] White, D. R., Saunders, P., Bonsey, S. J., van de Ven, J. and Edgar, H., "Reflectometer for Measuring the Bidirectional Reflectance of Rough Surfaces," *Appl. Opt.* 37(16), 3450-3454 (1998)
[11] Lequime, M., Zerrad, M., Deumie, C. and Amra, C., "A goniometric light scattering instrument with high-resolution imaging," *submitted to optics communications* (2008)
[12] Zerrad, M., Lequime, M., Deumie, C. and Amra, C., "Characterization of Optical Coatings with a CCD Angular and Spatial Resolved Scatterometer," in *Optical Interference Coatings*, p. ThA5, Optical Society of America (2007).
[13] Zerrad, M., Lequime, M., Deumie, C. and Amra, C., "Development of a goniometric light scatter instrument with sample imaging ability," in *SPIE Europe Optical Systems Design (Invited Paper)*, Glasgow, Scotland (2008).
[14] Deumié, C., Richier, R., Dumas, P. and Amra, C., "Multiscale roughness in optical multilayers: atomic force microscopy and light scattering," *Appl. Opt.* 35(28), 5583-5594 (1996)
[15] Maure, S., Albrand, G. and Amra, C., "Low-level scattering and localized defects," *Appl. Opt.* 35(28), 5573-5582 (1996)
[16] <http://www.superlumdiodes.com/pdf/s840-b-i-20.pdf>.
[17] <http://www.piacton.com/products/imcam/pixis/default.aspx>.
[18] <http://www.lw4u.com/super-eye-lens-tables.htm>.
[19] Zerrad, M., Deumié, C., Lequime, M. and Amra, C., "An alternative scattering method to characterize surface roughness from transparent substrates," *Opt. Express* 15(15), 9222-9231 (2007)
[20] Lequime, M., Abel, L. and Deumié, C., "Colorimetric properties of the light scattered by various objects," in *Proceedings of the SPIE The International Society for Optical Engineering. 25 Feb. 2004; 5250(1): 271-7* (2004).
[21] Gilbert, O., Deumié, C. and Amra, C., "Angle-resolved ellipsometry of scattering patterns from arbitrary surfaces and bulks," *Opt. Express* 13(7), 2403-2418 (2005)
[22] Amra, C., Zerrad, M., Siozade, L., Georges, G. and Deumié, C., "Partial polarization of light induced by random defects at surfaces or bulks," *Opt. Express* 16(14), 10372-10383 (2008)